RESEARCH ARTICLE

Figures and figure supplements

Functional implications of MIR domains in protein *O*-mannosylation

Antonella Chiapparino *et al*

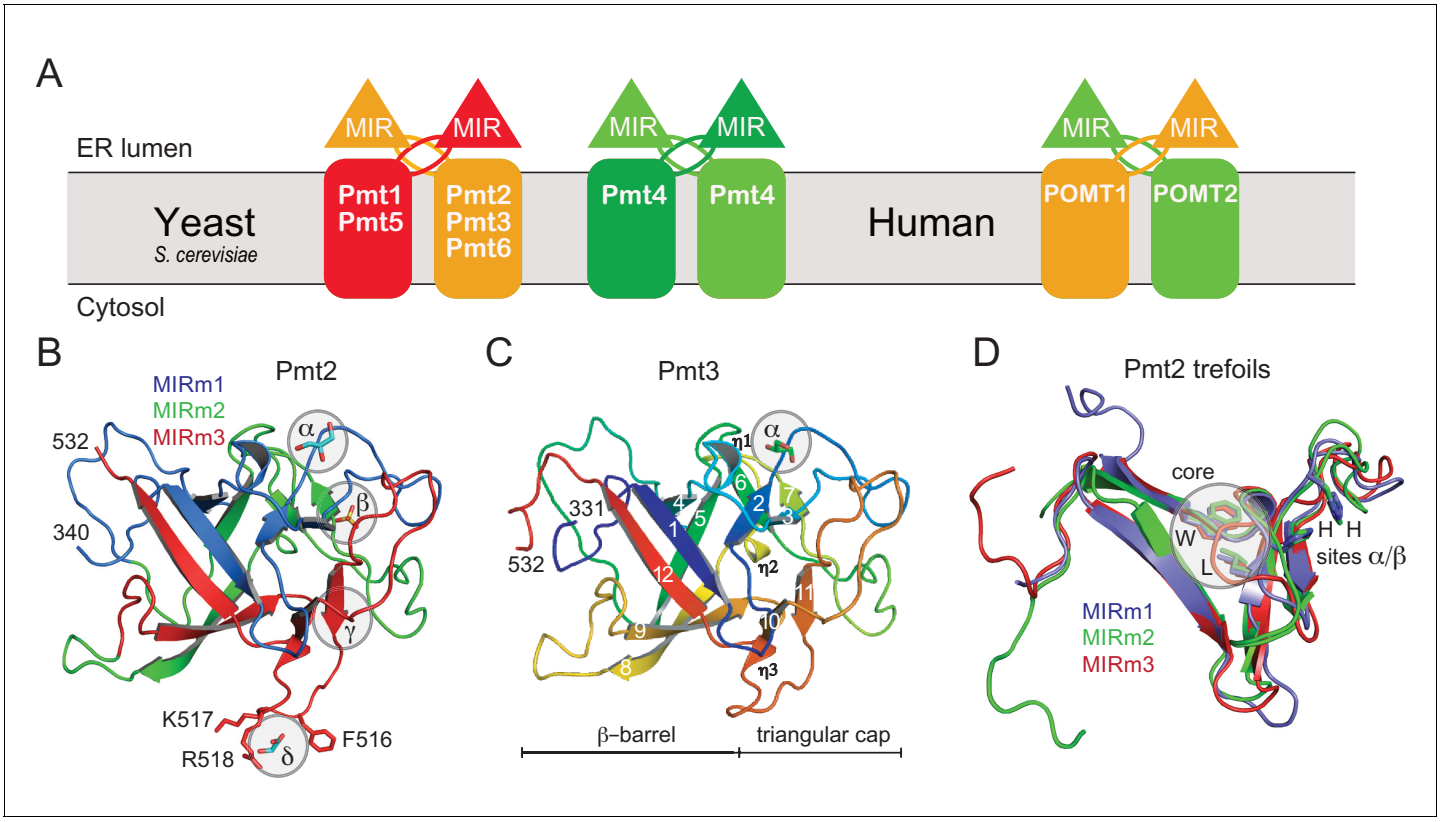

Figure 1. PMT-families and structure of PMT-MIR domains. (**A**) Schematic for the different PMT and POMT dimers. PMT1 (red), PMT2 (orange), and PMT4 (green) subfamilies are given together with the human homologs in the respective colors. In baker's yeast, PMT1 and PMT2 subfamily members form heterodimers, and Pmt4 homodimers. No partner is characterized for Pmt6. In mammals, the Pmt1 subfamily is not present. (**B**) Overall structure of Pmt2-MIR. Color coding is according to the MIR-motifs. Prominent ligand-binding sites (α to δ) are highlighted. (**C**) The structure of Pmt3-MIR is almost identical to Pmt2-MIR. Color coding is in a ramp from N- (blue) to the C-terminus (red). Secondary structures are labeled and identical in Pmt2-MIR. (**D**) Superposition of the three MIR-motifs (MIRm1-m3) in the same color as in panel A. Each MIRm contributes a tryptophane and a leucine residue to the conserved core of the MIR domain. Sites α/β, including two conserved histidine residues each, are only present in MIRm1 and MIRm2.

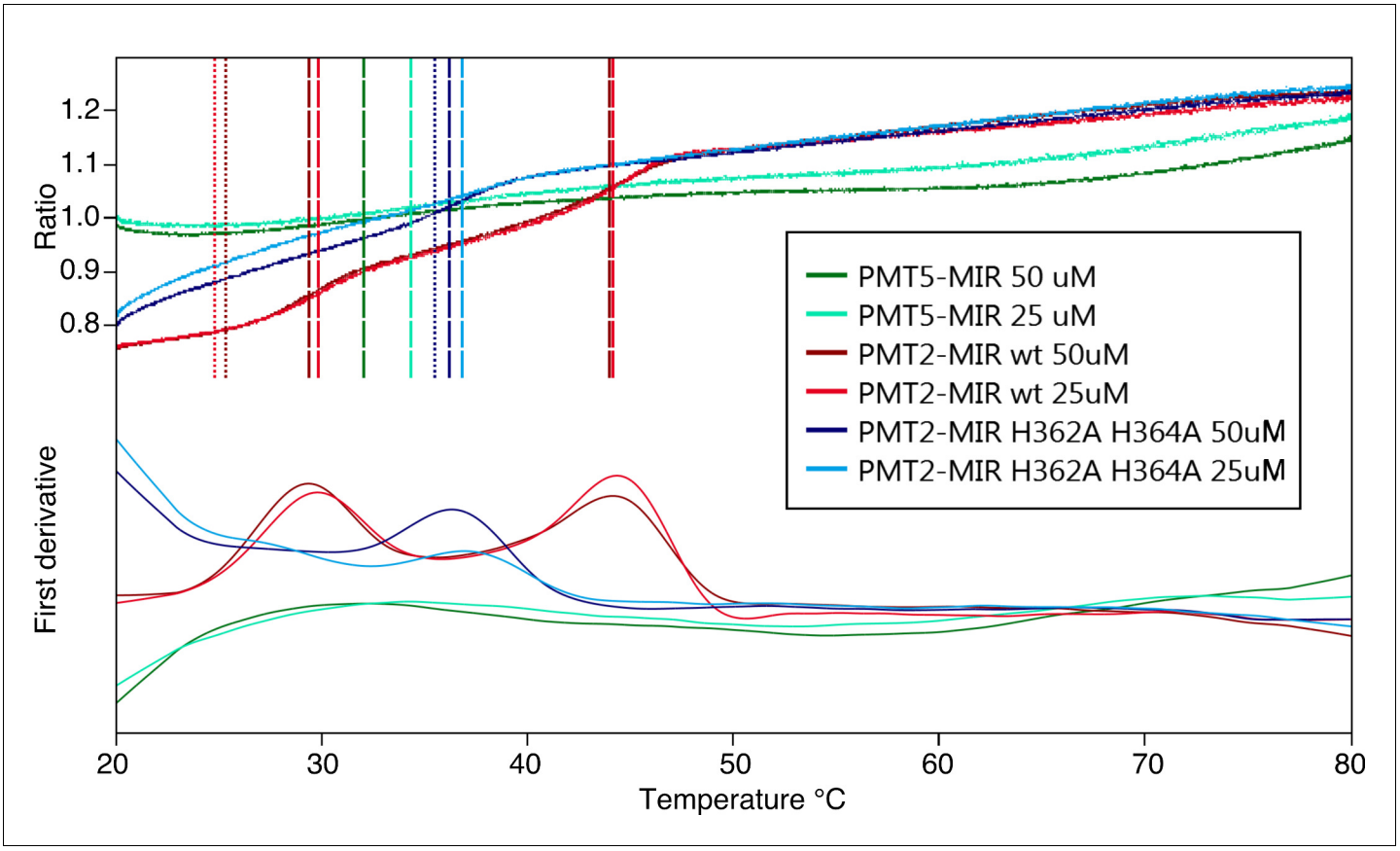

Figure 1—figure supplement 1. NanoDSF analyses of different Pmt-MIR domains. Data is shown for: Pmt2-MIR domain (red), its mutated variant (site α $H_{362}A$, $H_{364}A$, blue) and Pmt5-MIR domain (green). Melting temperatures (T_m) are calculated from peaks in the first derivative of the tryptophan fluorescence ratio (folded/unfolded). While Pmt2-MIR domain dissociates in two steps (two peaks), its mutant has an intermediate T_m, suggesting that the mutation perturbs its stability. Pmt5-MIR of the PMT1 family does not show any defined melting, suggesting that this protein is highly unstable.

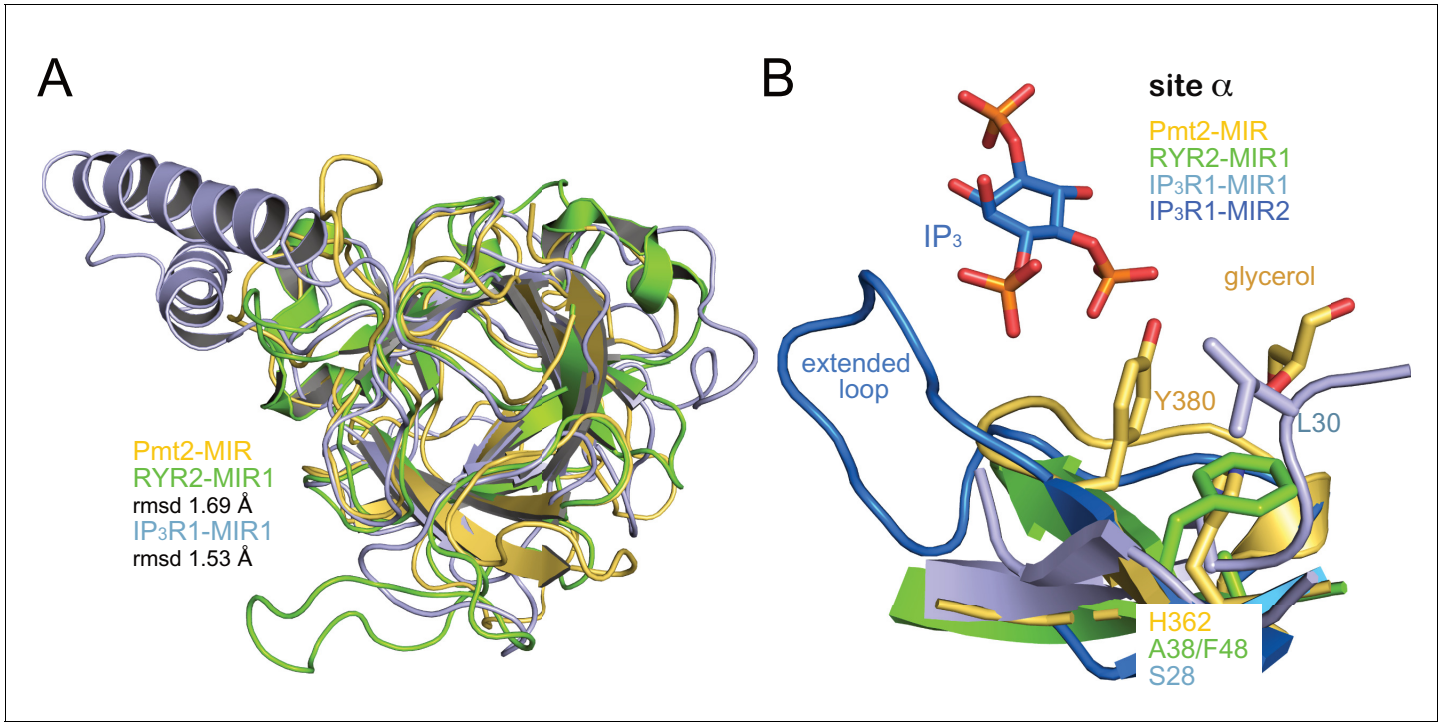

Figure 1—figure supplement 2. Comparison of MIR domains. (**A**) Superposition of MIR domains. Structures of MIR domains shown are: PMT2-MIR (yellow), human RyR2-MIR1 (green, PDB-ID 4jkq [***Borko et al., 2014***]) and rat IP_3R1-MIR1 (blue, PDB-ID 3uj0 [***Seo et al., 2012***]). The superposition is viewed along the pseudo-symmetric triad and deviations (rmsd) to PMT2-MIR are indicated. (**B**) Superposition of respective site α regions of different MIR domains. For Pmt2-MIR the crystal structure with bound glycerol is given. Sites α in MIR1 domains of RYR2 and IP_3R1 are blocked by indicated residues. Of note, an IP_3-ligand of IP_3R1 binds to an extended loop next to site α of a second MIR domain MIR2.

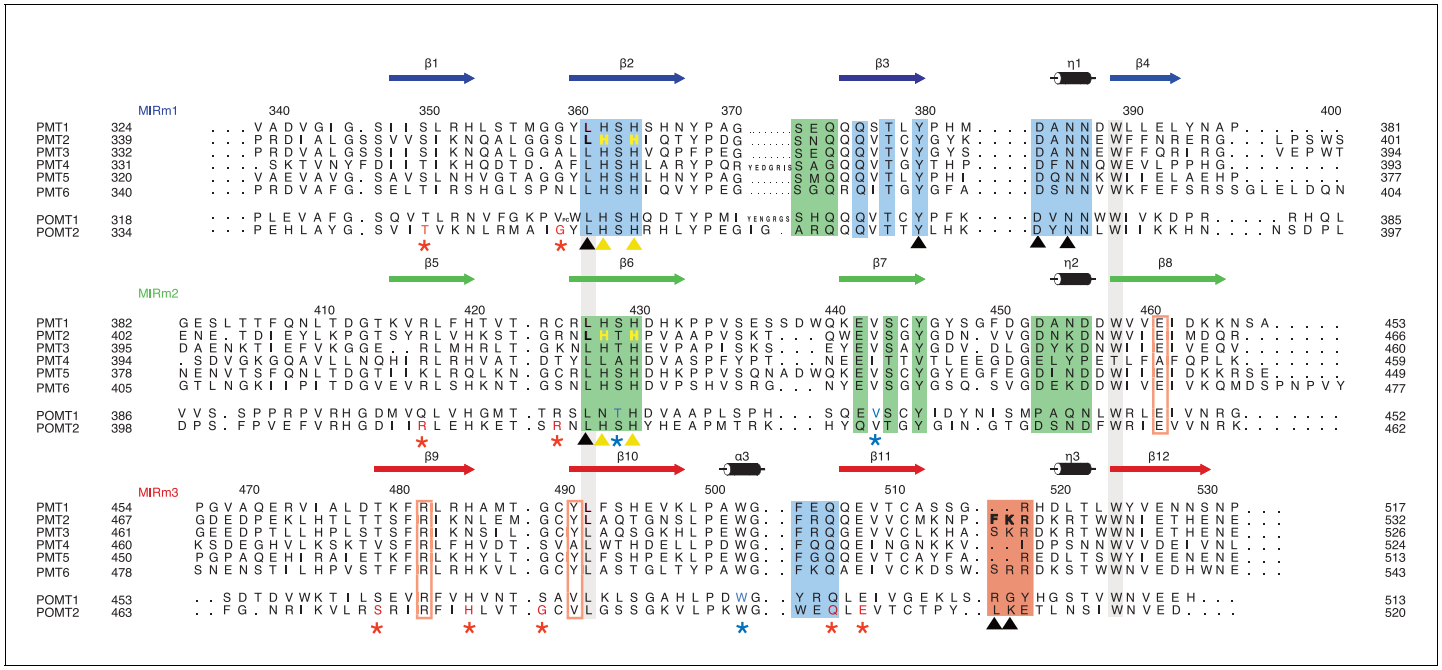

Figure 2. Sequence alignment of the PMT family. The alignment is structure-based for MIR domains of Pmt1, 2, and 3. Each line of the alignment corresponds to a MIR-motif and motifs are themselves aligned in order to highlight sequence conservations. Numbering and secondary structure above corresponds to Pmt2-MIR. The conserved leucine and tryptophane residues of the hydrophobic core in all MIR-motifs are highlighted by contiguous gray bars. Sites α, β, δ are highlighted by colored boxes and site δa by colored rectangles. Color code is according to ***Figure 1B***. Residues mutated in this study are highlighted and marked with yellow and black triangles. Residues causing human pathologies are highlighted for POMT1 and POMT2 and marked with blue and red asterisks, respectively. All mutated residues are highlighted with colors matching the triangle or asterisk symbols.

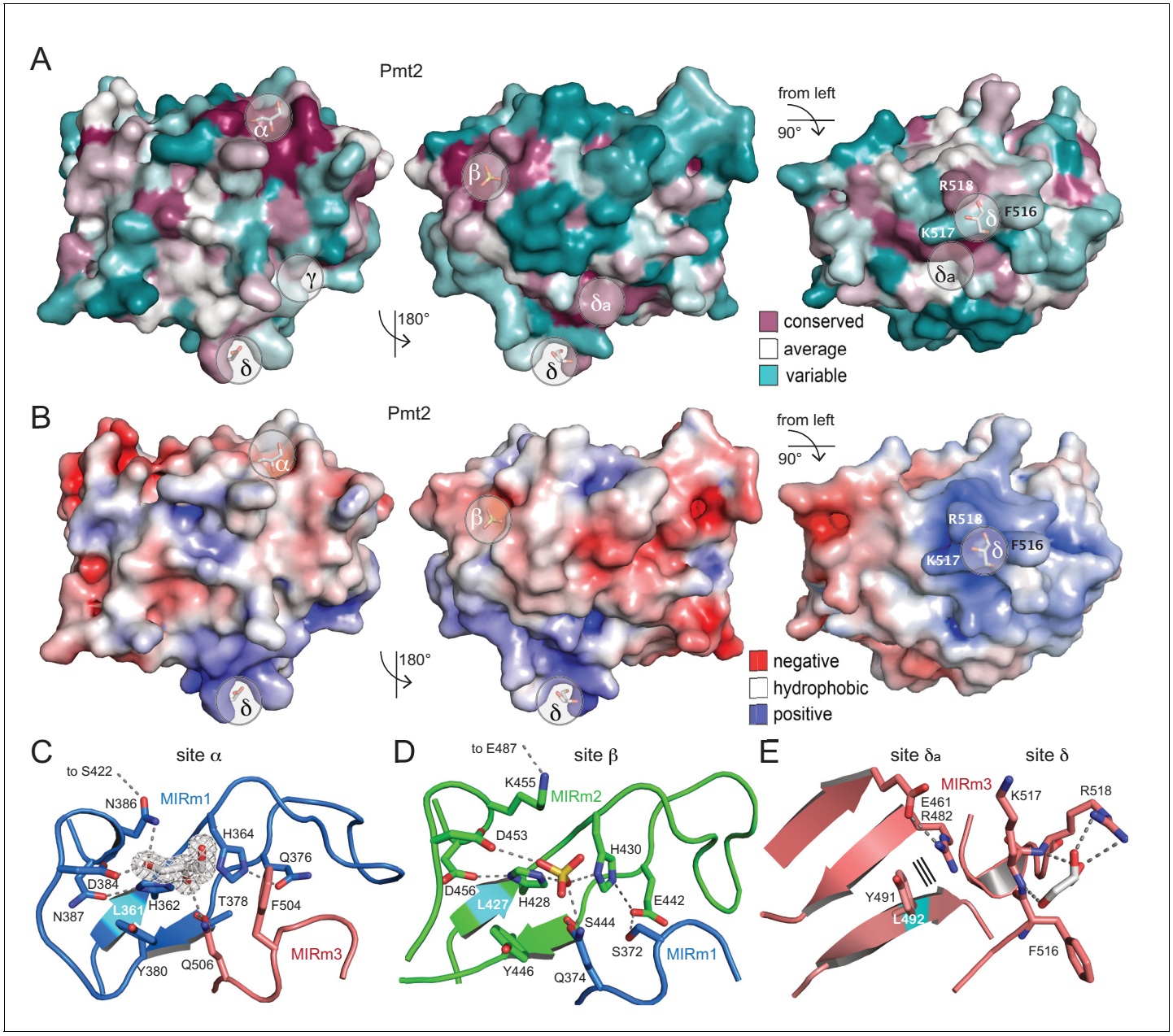

Figure 3. Surface properties and ligand-binding sites of Pmt2-MIR. (**A**) Surface conservation within the PMT family (increasing conservation from cyan over white to purple). Sites α, β, and δa correspond to regions of highest conservation, while sites γ and δ are PMT2-specific. (**B**) Same views for the electrostatic surface potential of Pmt2-MIR (±5 $_{k}$BT). While sites α and β are rather negatively charged (red), site δ forms a positively charged patch (blue). (**C**) The strictly conserved site α of the PMT family in the MIRm1/MIRm3 interface. Two highly coordinated histidines at the bottom of the cavity of the site are ligated to a glycerol ligand, which is shown within its $2mF_o$-DF_c electron density (2σ). Hydrogen bonds are shown by dashed lines. The conserved leucine of the core is highlighted in cyan. (**D**) The almost identical site β in the MIRm2/MIRm1 interface harbors a sulfate ion. (**E**) Pmt2-MIR-specific site δ and PMT-conserved site δa within MIRm3. Site δ forms a highly exposed trident (F516, K517, R518) that coordinates a glycerol molecule, while the adjacent site δa is ligand free. Parallel lines indicate stacking.

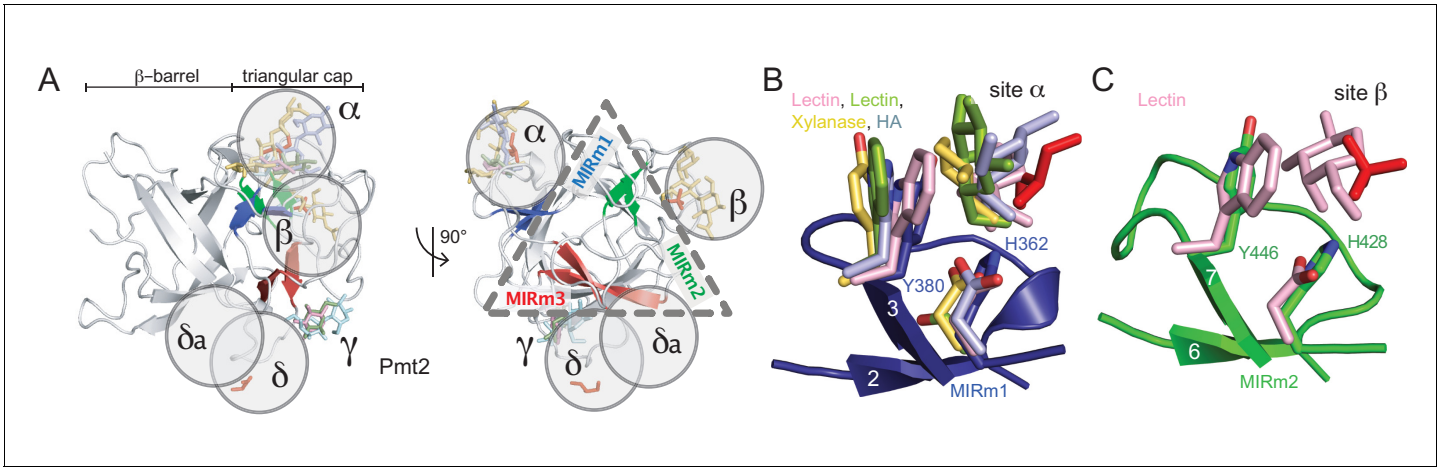

Figure 4. The MIR domain as carbohydrate-binding module (CBM). (**A**) The Pmt2-MIR domain is shown with only the β-strands within the triangular cap colored according the respective MIRm. Carbohydrate moieties bound to the α, β, and γ sites in β-trefoil CBM structures are superposed and shown together with the ligands bound to Pmt2-MIR sites α to δ (red). Each ligand-binding site locates to one lateral surface of the triangle. (**B**) Site α corresponds to a general carbohydrate-binding site and presents a conserved aromatic and a polar residue. (**C**) Although very similar to site α, site β is less frequently occupied by carbohydrate ligands.

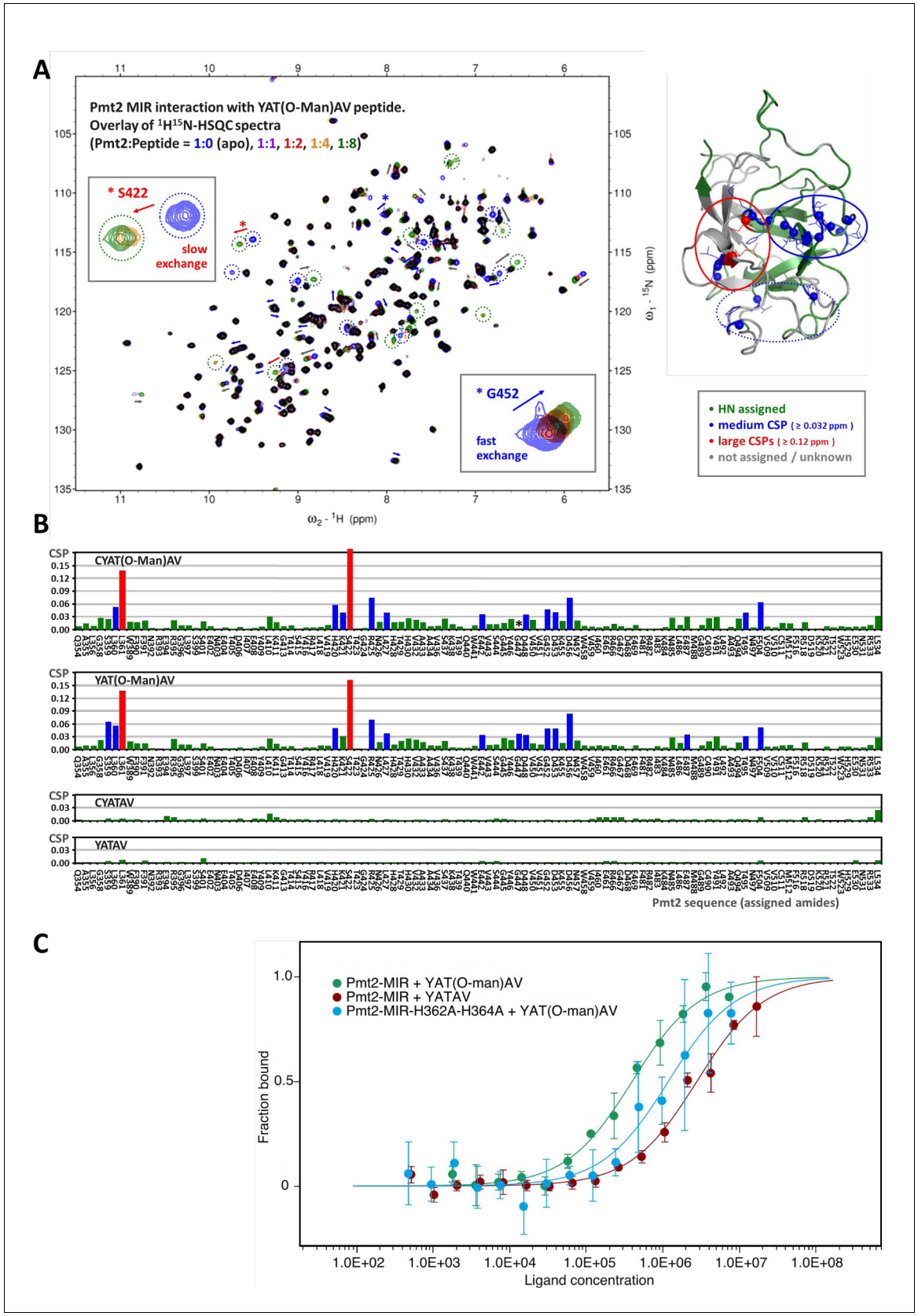

Figure 5. Characterization of O-Man peptide binding to Pmt2-MIR. (**A, B**) NMR analyses. (**A**) Interaction of Pmt2-MIR with the YAT(O-Man)AV peptide (NMR titration experiment using $^{1}H^{15}N$-HSQC spectra, left). Disappearing and new appearing signals and evident chemical shift perturbations (CSPs)

Figure 5 continued on next page

Figure 5 continued

indicate binding of the O-Man peptide. The most perturbed amide cross peaks are mapped onto the X-ray crystal structure (right) showing that mainly two (conserved) regions from MIRm1 and MIRm2 are involved (corresponding to sites α (in continuing red circle) and β (in continuing blue circle) albeit to a different extent. Interestingly, the backbone amides of some conserved leucine residues buried within the interior of the protein are also affected upon the interaction, hinting at indirect effects such as conformational changes within the protein upon substrate binding. (**B**) Pmt2-MIR interaction with O-Man and unmodified peptides. The CSPs for the Pmt2-MIR interaction with O-Man and unmodified peptides were obtained from NMR titration series ($^{1}H^{15}N$-HSQC spectra measured at Pmt2-MIR:peptide ratios of 1:0 (apo), 1:1, 1:2, 1:4, and 1:8). The combined $^{1}H^{15}N$ amide CSPs ($\Delta\delta HN = \sqrt{[(\Delta\delta H)^2 + (0.1\times\Delta\delta N)^2]}$, in ^{1}H ppm) are mapped on the sequence of Pmt2 showing no significant changes for the unmodified peptides and evident CSPs for the O-Man peptides (YAT(O-Man)AV and CYAT(O-Man)AV). An overall decrease of the amide signal intensity is observed for the Pmt2-MIR titration with the CYAT(O-Man)AV peptide (G447, marked with an asterisk, cannot be traced in the spectra as it disappears). (**C**) MST analysis of peptide substrate/product binding to Pmt2-MIR. The YATAV peptide and its O-Man product YAT(O-Man)AV are analyzed for Pmt2-MIR and its site α mutant lacking both conserved histidines ($H_{362}A$, $H_{364}A$).

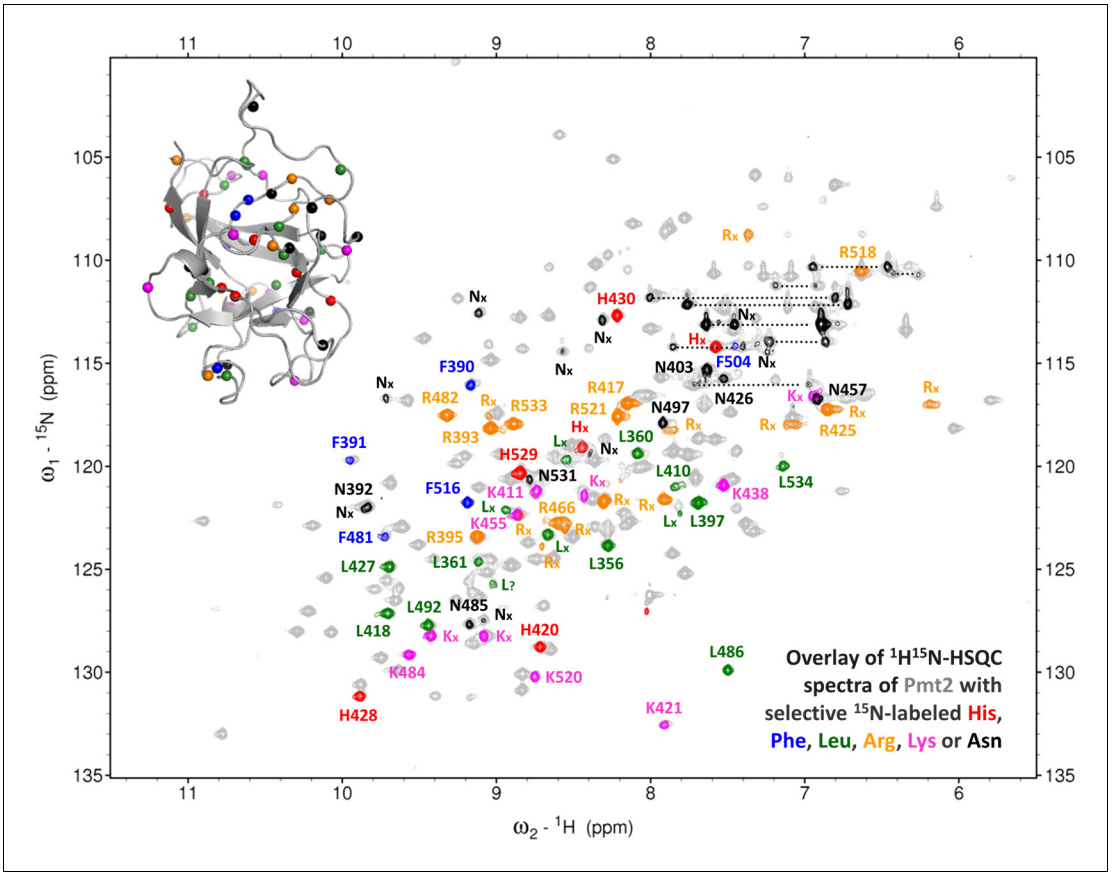

Figure 5—figure supplement 1. Selective ^{15}N-labeling of amino acids in Pmt2-MIR. Overlay of the ^{1}H^{15}N-HSQC spectra of uniform ^{15}N-labeled Pmt2-MIR domain (gray) with the ones in which selective amino acid are labeled (His in red, Phe in blue, Leu in green, Arg in orange, Lys in magenta and Asn in black). The backbone amide assignment is indicated (those which are ambiguous are marked with an x). The labeled amino acid positions are indicated (same color coding) in the inserted X-ray crystal structure of the MIR domain. The spectra of these selective labeled samples assist the NMR assignment and confirm the type of amino acid.

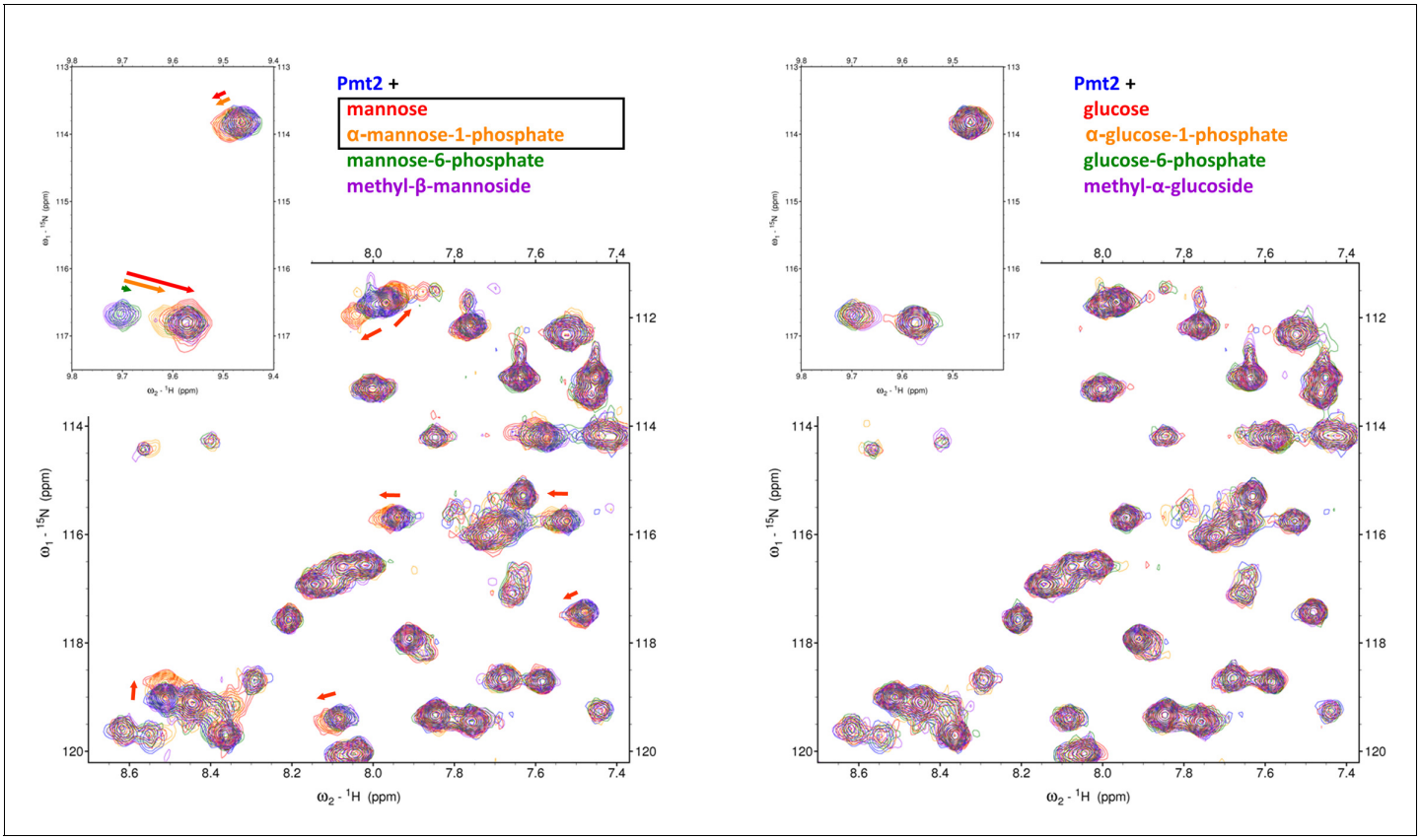

Figure 5—figure supplement 2. NMR screening of Pmt2-MIR sugar interactions. Pmt2-MIR spectra with several sugars are shown: mannose and derivatives (left) and glucose and derivatives (right). The presented regions from $^{1}H^{15}N$-HSQC spectra after addition of 55-times excess of the sugar (10 mM) are overlaid on top of the spectrum of apo-Pmt2-MIR (in blue). The evident CSPs for several Pmt2 amide signals show a specific (and comparable) interaction for mannose (left, in red) and α-mannose-1-phosphate (left, in orange), while the other sugars do not affect the spectrum of Pmt2-MIR.

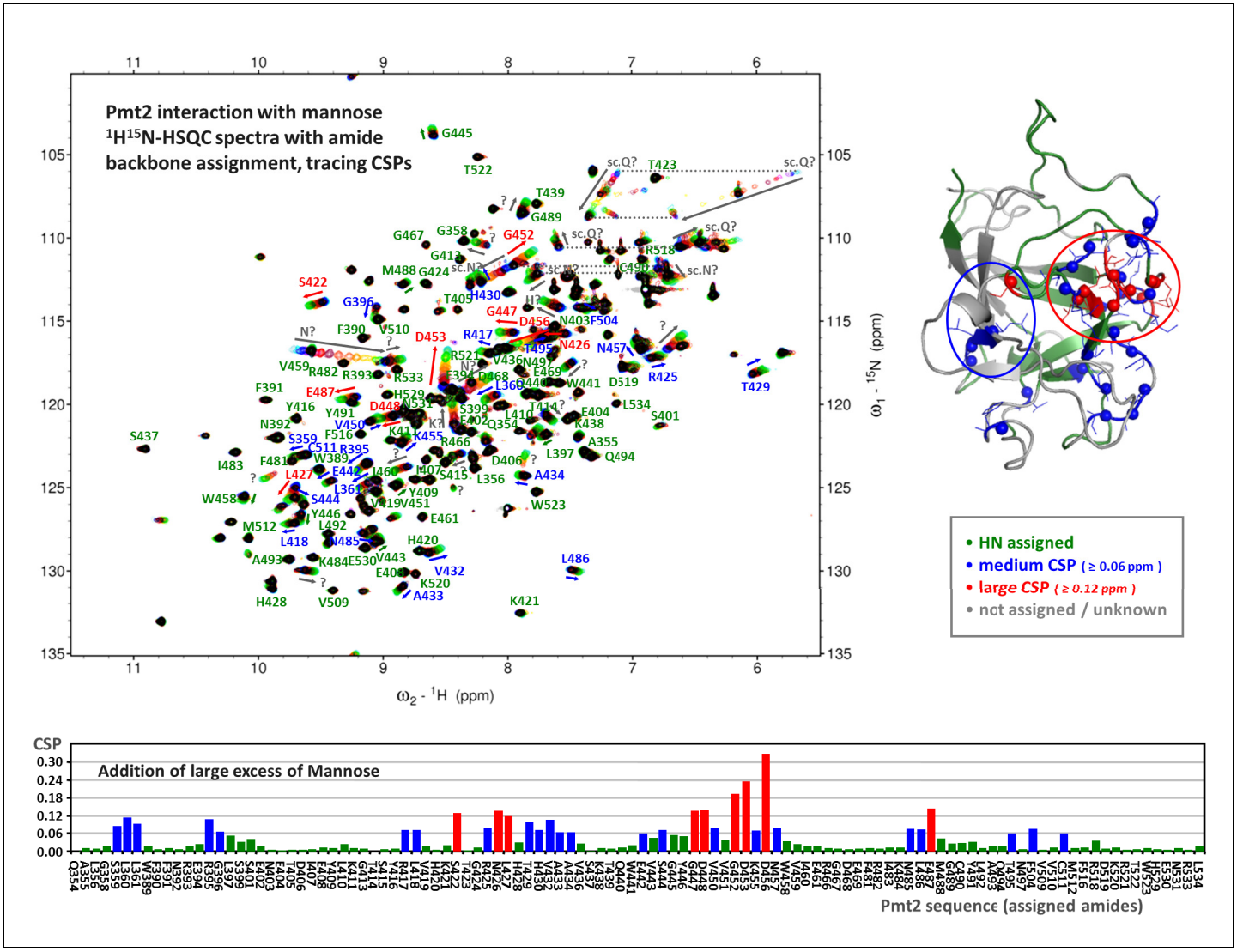

Figure 5—figure supplement 3. Pmt2-MIR interaction with mannose. Tracing Pmt2-MIR amide chemical shift perturbations (CSPs) from a titration series of $^{1}H^{15}N$-HSQC spectra (top left) to about 2000-fold excess of mannose (182 μM Pmt2-MIR protein and 376 mM mannose). The amide backbone assignment (about 56% completeness) is indicated and the main perturbations are indicated by arrows. The large CSPs and appearance of new signals indicate a weak (estimated K_D in 50–90 mM range), but specific interaction. The combined amide CSPs ($\Delta\delta HN = \sqrt{[(\Delta\delta H)^2 + (0.1\Delta\delta N)^2]}$) are mapped on the sequence of Pmt2 (bottom) and on the X-ray crystal structure of the MIR domain (top right) showing that two nearby regions are affected upon the interaction with mannose.

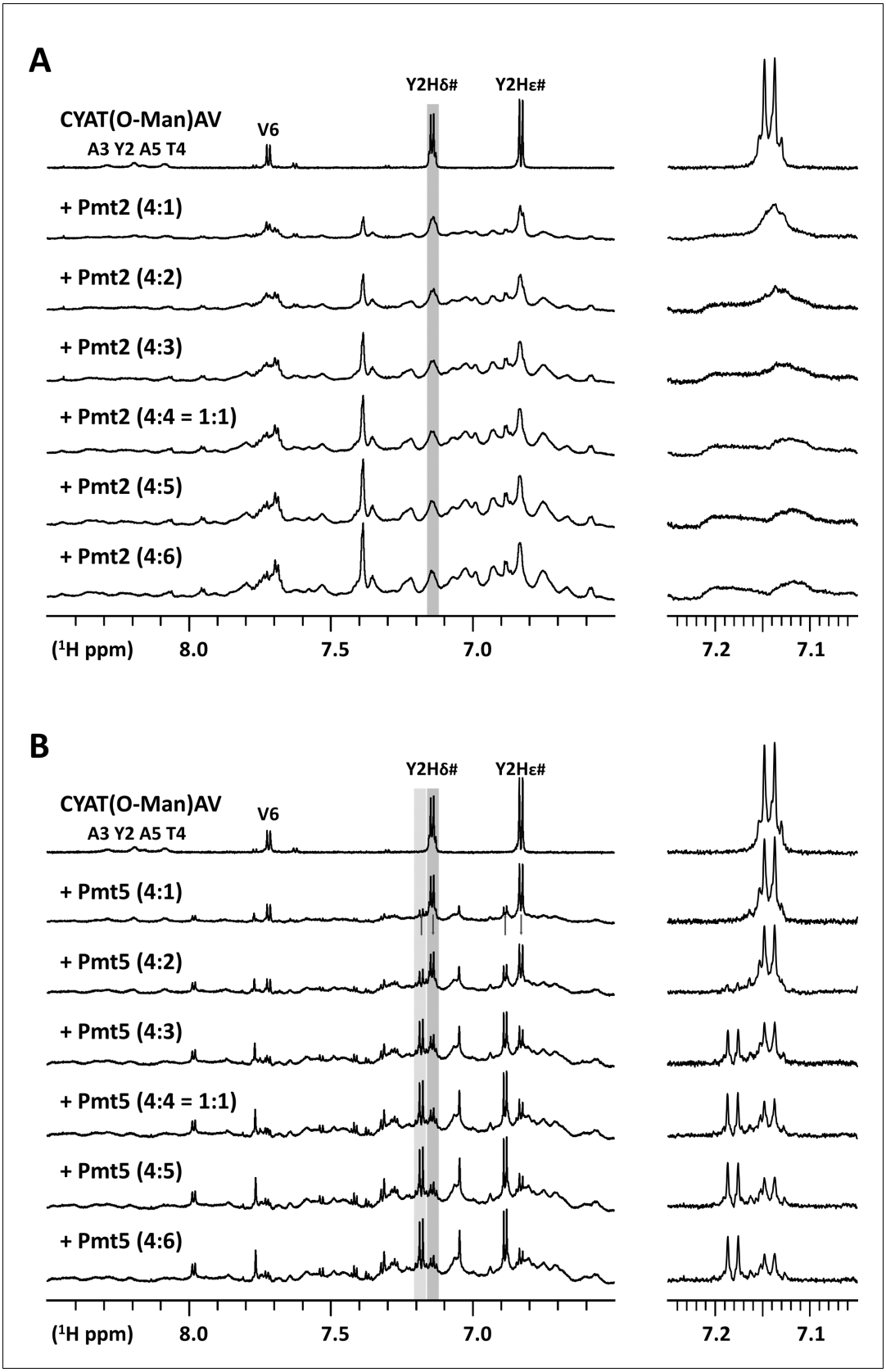

Figure 5—figure supplement 4. Interaction of Pmt2-MIR (A) and Pmt5-MIR (B) with the CYAT(O-Man)AV peptide. (**A**) The Pmt2-MIR domain strongly binds the CYAT(O-Man)AV peptide. Titration (1D ^{1}H NMR) of the CYAT(O-Man)AV peptide with Pmt2 protein to a 1.5 times excess (4:6). The proton 1D

Figure 5—figure supplement 4 continued on next page

Figure 5—figure supplement 4 continued

spectra on the left shows the amide and aromatic region. The signals from Pmt2-MIR come up while the signals of the peptide broaden out and disappear upon addition of the protein as also visualized by the expanded region on the right showing the disappearance of the peptide Tyr-2 $H_{\delta\#}$ signal (after background-subtraction of a blank apo-Pmt2 spectrum of the same concentration). (**B**) The Pmt5-MIR domain binds the CYAT(O-Man)AV peptide in slow exchange. Titration (1D ^{1}H NMR) of the CYAT(O-Man)AV peptide with Pmt5-MIR protein to a 1.5 times excess (4:6). The proton 1D spectra on the left shows the amide and aromatic region. The signals from Pmt5-MIR come up while the aromatic tyrosine signals of the peptide disappear and appear at a new position upon addition of the protein as also visualized by the expanded region on the right showing the peptide Tyr-2 $H_{\delta\#}$ signal (after background-subtraction of a blank apo-Pmt5-MIR spectrum of the same concentration).

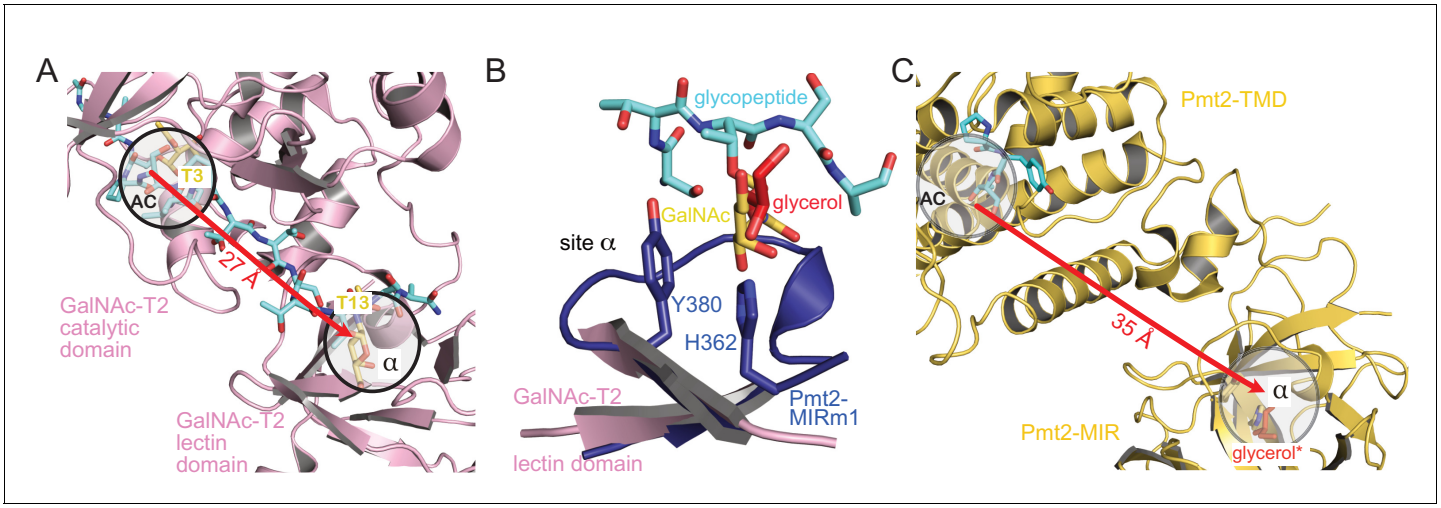

Figure 6. Analogy of β-trefoils in Pmt2 and GalNAc-T2. (**A**) Spatial correlation of the active center (AC) and site α within the lectin domain of human GalNAc-transferase 2 (pink) bound to a GalNAc-glycopeptide (PDB-ID 5ajo [***Lira-Navarrete et al., 2015***]). Both sites are occupied by GalNAc moieties (yellow) attached to threonine T3 and T13 of the glycopeptide (cyan), respectively. The site distance is indicated by a red arrow. (**B**) Superposition of Pmt2-MIRm1 site α (blue) with the lectin domain of human GalNAc-T2. The glycerol (red) within Pmt2-MIRm1 site α overlaps with the GalNAc moiety of the glycopeptide. (**C**) Spatial arrangement of the AC within the Pmt2-TMD in respect to site α of Pmt2-MIR in the Pmt1-Pmt2 complex (PDB-ID 6p25 [***Bai et al., 2019***]). Pmt2-TMD is bound to the PYTV-peptide, and Pmt2-MIR site α is shown occupied with glycerol as found in the Pmt2-MIR X-ray structure (red, superposition denoted by an asterisk). The site distance is similar to GalNAc-T2.

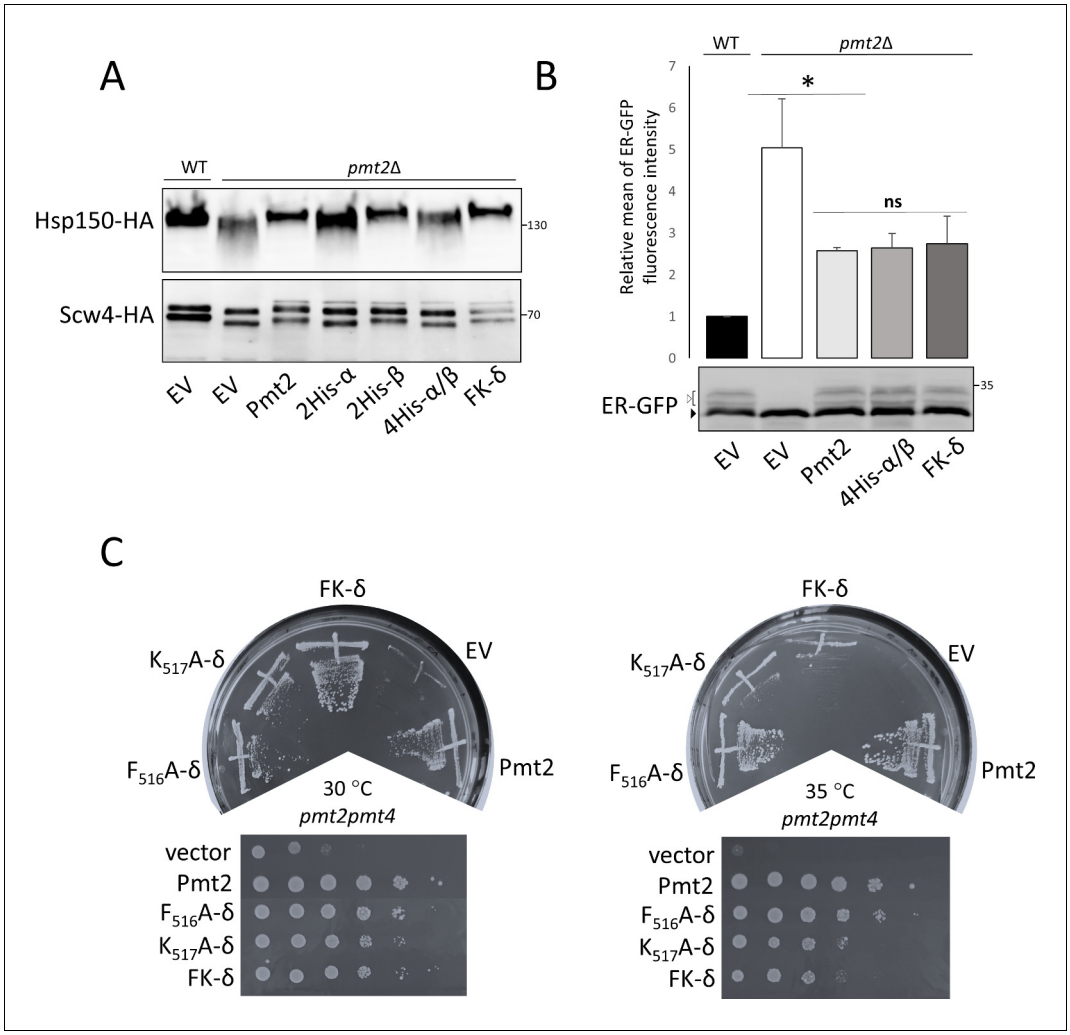

Figure 7. Functional characterization of Pmt2-MIR in vivo. (**A-C**) Analysis of yeast strains expressing a vector control (YEp352; empty vector; EV) or HA-epitope tagged versions of wild type Pmt2 (pVG80) or mutant thereof with alanine substitutions in site α (2His-α: $H_{362}A$, $H_{364}A$ (pAG1)), site β (2His-β: $H_{428}A$, $H_{430}A$ (pAG2)) and in combination (4His-α/β: $H_{362}A$, $H_{364}A$, $H_{428}A$, $H_{430}A$ (pAG4)), as well as in site δ ($F_{516}A$ (pAG7); $K_{517}A$ (pAG8); FK-δ: $F_{516}A$, $K_{517}A$ (pAG9)). (**A**) *O*-mannosylation status of canonical Pmt1-Pmt2 substrates Hsp150 (upper panel) and Scw4 (lower panel). Indicated constructs were expressed in *pmt2*Δ mutants expressing HA-tagged Hsp150 (strain AGY15, upper panel) or Scw4 (strain *pmt2*Δ transformed with YEp351a, lower panel). Hsp150 and Scw4 were isolated and analyzed by Western blot as detailed in Material and methods. Molecular weight marker is indicated on the right. (**B**) Analysis of the *O*-mannosylation status of the UPOM substrate ER-GFP by FACS (upper panel) and Western blot (lower panel). Indicated constructs were expressed in a wild type strain (BY4741; WT) or a *pmt2*Δ mutant (Y00386). Upper panel: Fluorescence intensities of the strains are shown, indicating the degree of *O*-mannosylation of ER-GFP. The mean fluorescence intensity value of WT strain was taken as reference and set to one. Statistical analysis was performed using t-test at the significance level p<0,05 (*). Abbreviation *ns* stands for not significant. Lower panel: Different glycosylated variants of ER-GFP are visible (black and white arrows) that have been described previously (***Castells-Ballester et al., 2019***). (**C**) Complementation of thermosensitive phenotype of *pmt2pmt4* mutant transformed with the indicated constructs. Thermosensitivity of the strains was assessed 45 hr after the inoculation by comparing yeast grown at 30˚C and 35˚C. Tenfold serial dilutions, starting from 10^6, are shown in lower panels.

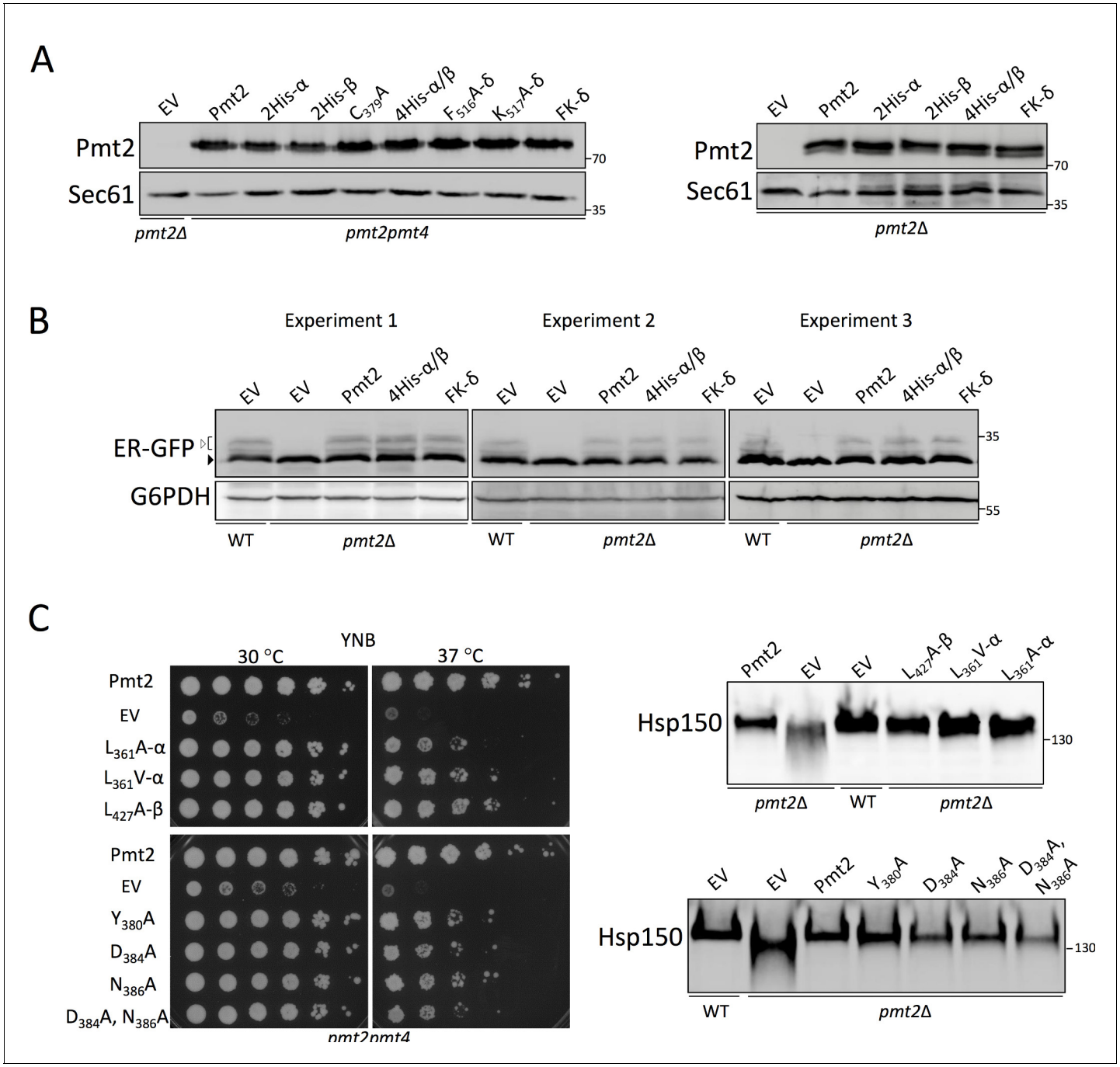

Figure 7—figure supplement 1. Characterization of Pmt2 alanine-exchange mutants. (**A**) Protein levels of Pmt2 mutant proteins. HA-epitope tagged Pmt2 wild type and alanine exchange mutant proteins were expressed in pmt2Δ or pmt2pmt4 deletion strains as indicated and grown at 30˚C (left panel) and 37˚C (right panel). YEp352 served as vector control (empty vector, EV). 70 µg (left panel) and 40 µg (right panel) of total membrane proteins were resolved on 8% polyacrylamide gels and analyzed by Western blot. Pmt2 proteins were detected by HA-tag directed antibody. Sec61 served as loading control. (**B**) *O*-mannosylation status of the UPOM substrate ER-GFP. Cell extracts were obtained from indicated strains, as described in Materials and methods. 50 µg (Experiment1), 75 µg (Experiment 2) or 100 µg (Experiment 3) of protein from total whole cell extracts was resolved on a 12% polyacrylamide gel and analyzed by Western blot. G6PDH served as a loading control. Black arrow (left) indicates the main ER-GFP band, white arrow (left) marks *O*-mannosylated ER-GFP forms. Two biological replicates (Experiment 1 and Experiment 2) and one technical replicate (Experiment 3, a technical replicate of Experiment 2) are shown. Experiment 1 is also shown in ***Figure 7B***. (**C**) In vivo analysis of the functionality of different mutants in the PMT2-MIR domain. Analysis of PMT2-HA with individual alanine substitutions of leucine residues in MIRm1 ($L_{361}A$; pJS4, $L_{361}V$; pJS6) and MIRm2 ($L_{427}A$; pJS6), and of mutants in MIRm1 covering the conserved sequence fingerprint 384-DxNN (pAS151-154). Left panel: Complementation of thermosensitive phenotype (growth on YNB; 37˚C) of *pmt2pmt4* mutant strains expressing either wild type Pmt2, EV (YEp352) or respective Pmt2

Figure 7—figure supplement 1 continued on next page

Figure 7—figure supplement 1 continued

version with indicated mutation. Right panel: Analysis of the glycosylation status of Hsp150 in indicated strains. Enriched protein fractions were resolved on 8% polyacrylamide gels and analyzed by Western blot decorated with Hsp150-HA tag directed antibodies. In all panels, the position of the molecular weight marker is indicated on the right.

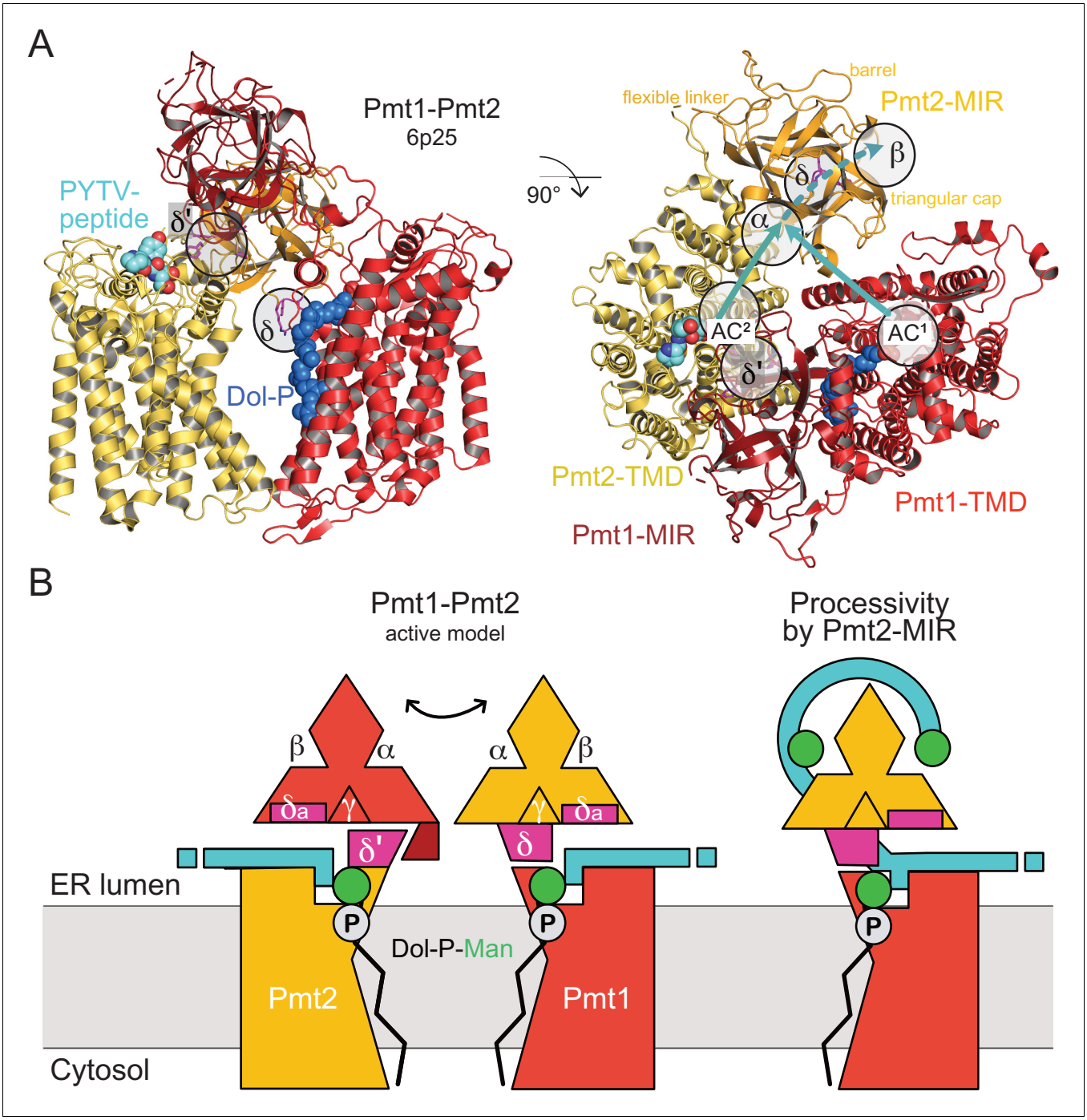

Figure 8. MIR domain function in protein *O*-mannosylation. (**A**) Cryo-EM structure of the yeast Pmt1-Pmt2 complex (PDB-ID 6P25 [***Bai et al., 2019***]). Substrate-peptide fragment and dolichol-phosphate (Dol-P) are bound to different subunits and MIR domain orientation is asymmetric. ligand-binding sites and the location of the active sites of Pmt1 and Pmt2 (AC^1, AC^2) are indicated. Putative trajectories of mannosylated peptides from both ACs to site α and subsequently site β within Pmt2 are indicated by cyan arrows. Site δ (magenta, FKR shown in sticks) might functionally correspond to site δ′ of Pmt2-TMD involved in Pmt1-MIR interactions. (**B**) Schematic models for active Pmt1-Pmt2 dimer and for Pmt2-MIR processivity. Left: Sites δ and complementary δ′ mediate alternate TMD-MIR domain interactions (domain dynamics indicated by double-arrow). Sites δa might interact with the substrate (cyan). Right: Sites α and β of Pmt2-MIR bind to the mannosylated peptide thus organizing the active center of Pmt1 for processive reaction.

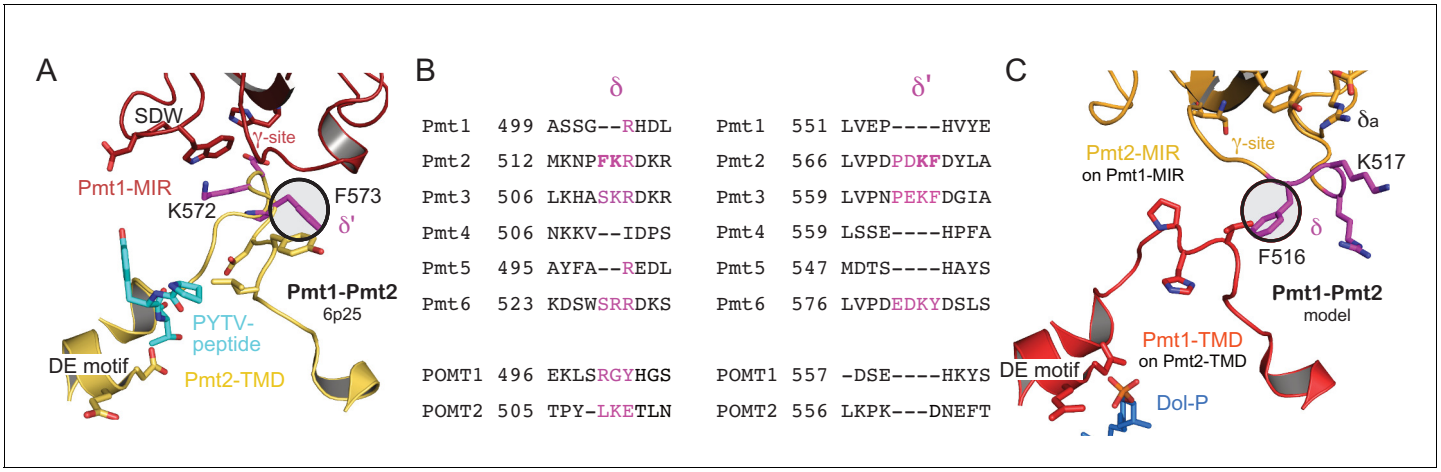

Figure 8—figure supplement 1. Domain interactions in the Pmt1-Pmt2 heterodimer. (**A**) The Pmt2-TMD/Pmt1-MIR contact in the cryo-EM Pmt1-Pmt2 structure (***Bai et al., 2019***). Site γ and the PMT1-specific SDW insertion in Pmt1-MIR mediate the sole contact with the Pmt2-TMD at site δ′ (magenta) within the LL4 loop next to the active center (indicated by the catalytic DE motif and the bound peptide). (**B**) Sequence alignment of the PMT/POMT family for sites δ and δ′ (magenta) and surrounding sequences only. The mirrored FK/KF sequences for Pmt2 are highlighted in bold type. (**C**) Model for the corresponding Pmt1-TMD/Pmt2-MIR contact based on respective domain superposition. Site δ matches to site δ′ and the corresponding phenylalanines superpose exactly (encircled). The adjacent site δa is indicated.

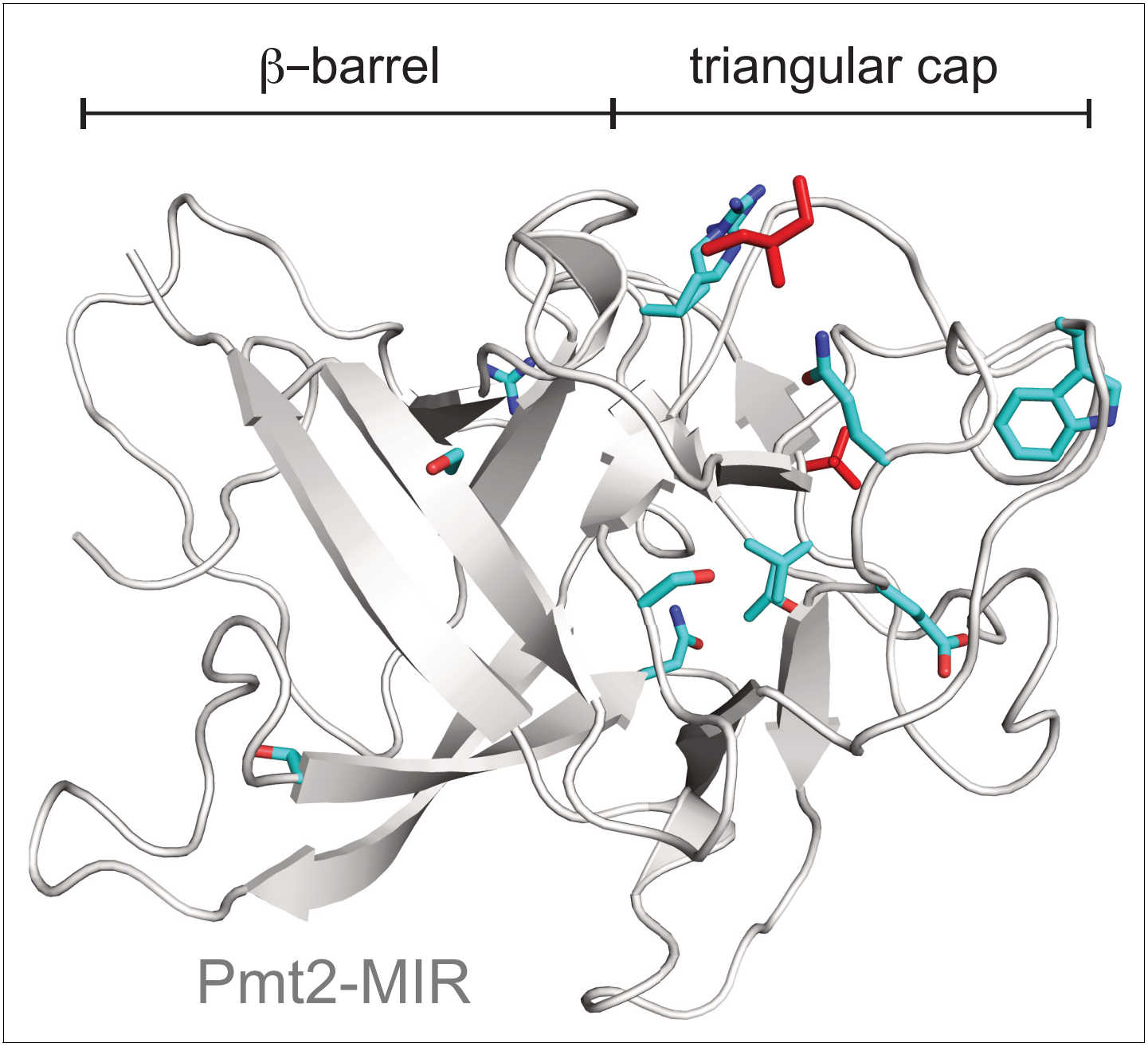

Figure 8—figure supplement 2. Missense mutation sites in human POMT1/2. The missense mutations (cyan) causing α-dystroglycanopathies are projected onto the Pmt2-MIR structure (gray) with bound ligands in sites α and β (red).